Nuclear Materials and Energy 27 (2021) 100999

Contents lists available at ScienceDirect

Nuclear Materials and Energy

journal homepage: www.elsevier.com/locate/nme

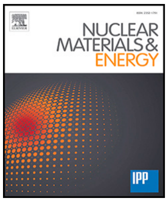

Plasma edge simulations including realistic wall geometry with SOLPS-ITER

W. Dekeyser [a,*], P. Boerner [b], S. Voskoboynikov [c], V.A. Rozhanksy [c], I. Senichenkov [c], L. Kaveeva [c], I. Veselova [c], E. Vekshina [c], X. Bonnin [d], R.A. Pitts [d], M. Baelmans [a]

[a] KU Leuven, Department of Mechanical Engineering, Celestijnenlaan 300, 3001 Leuven, Belgium
[b] Institute of Energy and Climate Research (IEK-4), Forschungszentrum Juelich GmbH, Juelich, D-52425, Germany
[c] Peter the Great St.Petersburg Polytechnic University, St.Petersburg, Russia
[d] ITER Organization, Route de Vinon-sur-Verdon, CS 90 046, 13067 St Paul Lez Durance, France

ARTICLE INFO

Keywords:
SOLPS-ITER
Divertor modeling
Extended grids
Unstructured finite volume solver

ABSTRACT

In plasma edge simulations using the SOLPS-ITER code, the simulated Scrape-Off Layer plasma domain has historically been restricted to magnetic flux surfaces contacting divertor targets at both ends. We present here a newly developed numerical solver for the B2.5 plasma solver in SOLPS-ITER, allowing the numerical grid to be extended to the true vessel boundaries. The new, unstructured Finite Volume scheme can deal with arbitrary grids and magnetic topologies in the 2D poloidal plane. It includes a correct numerical treatment of possibly misaligned faces and cells w.r.t. the magnetic field to cope with, for example, strong divertor target shaping. The solver combines the benefits of an accurate numerical separation of fast parallel and slow radial transport, with a realistic description of the wall geometry, and the possibility of local grid refinement to capture sharp features in the Scrape-Off Layer flows. Generalized sheath boundary conditions are presented that can be imposed at all vessel boundaries, removing an important modeling uncertainty related to the specification of *ad hoc* decay length boundary conditions at the outer flux surfaces. The resulting model is applied to an AUG single-null case, a standard benchmark case for SOLPS-ITER. We analyze in particular the impact of the extended plasma model on upstream and divertor plasma conditions, and the improved predictions of heat and particle loads to the main chamber wall. The extended solver also allows for a much improved qualitative agreement between fluid and kinetic neutral simulations, because the fluid neutral solution, which is obtained on the plasma grid, now also extends to the true main chamber and divertor vessel boundaries.

1. Introduction

The SOLPS-ITER [1,2] code suite is presently the most widely used package for plasma edge modeling in the magnetic fusion community. It interprets exhaust scenarios in most existing devices, and supports the design of future devices, such as ITER [3,4], DEMO [5] or CFETR [6]. One of the important limitations of the package thus far has been the restriction of the simulated Scrape-Off Layer (SOL) plasma domain to magnetic flux surfaces contacting divertor targets at both ends, covering only the near-SOL region and a limited part of the divertor. At the same time, modeling uncertainty is introduced by the need to specify rather arbitrary decay length or leakage type boundary conditions (BCs) at these last simulated flux surfaces. While this approach is generally assumed sufficiently reliable to accurately model the particle and heat loads at the divertor targets, it prohibits an accurate assessment of particle and heat loads to the other plasma-facing components such as the main chamber wall, upper part of the baffles, and the dome, taking the particular example of the ITER tokamak. Moreover, an assessment of far-SOL flows, which play a key role in material erosion, migration, and re-deposition studies, is precluded without a numerical grid extending to the wall surfaces.

Options to extend the plasma grid to the vessel boundary have previously been implemented in SOLPS code versions, first in SOLPS4 [7,8] and later also in SOLPS5.0 [9], but were not yet included in SOLPS-ITER. These implementations followed a so-called cut-cell approach, where the code internally relies on topologically structured, orthogonal grids extending beyond the vessel, but cells outside of the vessel are ‘isolated’ or removed from the computations. To our knowledge, only a few other plasma edge codes have developed extended grid capabilities. SOLEDGE2D-EIRENE [10] also relies on structured, field-aligned grids extending beyond the vessel boundaries. It implements realistic wall geometries by identifying parts of the grid outside of the actual vessel by a mask function, and forcing the plasma density and momentum to zero in those cells through a penalization scheme in a finite volume setting. In Ref. [11] a higher order HDG (Hybrid Discontinuous

---

[*] Corresponding author.
E-mail address: wouter.dekeyser@kuleuven.be (W. Dekeyser).

https://doi.org/10.1016/j.nme.2021.100999
Received 30 December 2020; Accepted 1 April 2021
Available online 9 April 2021

Galerkin) approach is used for plasma edge simulations in realistic geometries. Due to the higher order schemes, fully unstructured, non-aligned grids can be used, which opens up the possibility to simulate varying magnetic field configurations without the need for remeshing. However, at present the physics model implemented in the HDG code is less complete than that of SOLPS-ITER or SOLEDGE2D-EIRENE. Also the TOKES code [12], developed at KIT, has full grids to the walls and options for adaptive grids, but has no kinetic neutral package.

In this contribution, we present a newly developed numerical solver for the B2.5 plasma solver in SOLPS-ITER, allowing the numerical grid to be extended to the true vessel boundaries. The scheme generalizes the extended grids capability developed for older SOLPS code versions [7–9] towards unstructured, finite volume grids. This enables full flexibility for the resolution of wall features and complex magnetic topologies. It includes a correct numerical treatment of possibly misaligned cells w.r.t. the magnetic field to cope with, for example, strong divertor target shaping [13].

The paper discusses the basic principles underlying the new extended grids solver. Section 2 motivates the choice to move towards a fully unstructured finite volume approach for SOLPS-ITER, by comparing with existing extended grid approaches for B2(.5) and identifying remaining issues and bottlenecks. Section 3 describes the main aspects of the discretization of the governing plasma equations on arbitrary, unstructured grids. Generalized sheath boundary conditions and the coupling with kinetic neutrals are described in Sections 4 and 5 . In Section 6, the new solver is applied to extended grid simulations for a reference AUG case, including, for the first time, coupled B2.5-EIRENE extended grid simulations. Finally, conclusions and perspectives are summarized in Section 7.

2. Unstructured finite volume grids for plasma edge simulations

The first implementations of extended grid options in SOLPS code versions followed a cut-cell approach [7–9]. A structured, fully orthogonal grid is first constructed that extends beyond the vessel walls, after which the actual geometry is introduced by ‘cutting’ through these orthogonal cells. As a result, only cells in contact with the boundary are not perfectly aligned with the magnetic field, in the sense of having two faces aligned with and two faces orthogonal to the poloidal projection of the magnetic field. An example of such a grid for the ASDEX Upgrade (AUG) tokamak, constructed with CARRE2, is given in Fig. 1 (right) [9]. Cells in contact with the vessel are indicated in green. This approach allows the plasma up to the vessel wall to be described with relatively small adaptations to the code: the grid remains topologically rectangular, with cells outside of the actual vessel simply ‘isolated’ or removed from the computation. Modifications to the computation of fluxes are only needed in cells/faces near the boundaries. However, there are several drawbacks to this approach. Due to the restriction to structured grids with orthogonal internal grid lines, and the need to avoid cells with more than 4 faces at boundaries, poloidal and radial grid resolutions near boundaries cannot be controlled independently, but are determined by the local surface inclination. In addition, obtaining good resolution of gradients developing towards the sheath is challenging. This results in very large cell numbers in the divertor, and unnecessarily high resolution in other grid areas (e.g. upstream). Moreover, simulating advanced divertor configurations with multiple and/or higher-order X-points is challenging in this structured approach.

Locally improving the grid resolution near boundaries can be achieved by aligning (poloidal) faces with the surface instead of with the field, as is currently often done near divertor targets (see Fig. 1 (left)). Hence, it is reasonable to consider a combination of a cut-cell approach with grid deformation to combine the benefits of both approaches. However, as seen in Fig. 1, the combination of mesh alignment with the targets and strong target shaping often leads to ‘bunching’ of field lines near the top of the baffles. Similar effects of ‘bunched’ grid lines appear due to the presence of an X-point, both in the orthogonal and misaligned grid approaches (Fig. 1). This grid line bunching again leads to unnecessarily high resolution in some parts of the grid (e.g. near the top of the baffles), and also leads to numerical difficulties due to rapidly varying cell sizes.

To avoid effects such as grid line bunching, a fully unstructured grid approach is the most promising. Two illustrative examples are given in Fig. 2. The left figure shows how the use of a few triangular cells internal to the domain allows a good, uniform poloidal resolution in the entire divertor leg to be achieved even in the presence of strong target shaping. The right figure shows how the use of pentagonal cells in the vicinity of the X-point permits good spatial resolution at the X-point, without bunching field lines further away. These kinds of unstructured grids also provide the largest flexibility to resolve geometrical features in the wall geometry, complex magnetic topologies (e.g. snowflake, X and super-X divertors), and naturally enable more advanced grid features such as boundary layer grids, local grid refinement, and adaptive grid refinement. Based on these considerations, it was decided to convert the B2.5 plasma solver into a fully unstructured finite volume solver, that allows for arbitrary polygonal cell shapes with arbitrary orientation of each cell face w.r.t. the magnetic field.

While the new unstructured solver can treat a wide range of complex grids and magnetic topologies, a word of caution is needed. It is by no means recommended to switch, for example, to pure triangulations of the simulated domain. The numerical discretization (see Section 3) is still based on hybrid schemes, which are second order in space for diffusion-dominated flows, but revert to first order for convection-dominated cases. The combination of these low-order schemes with the large anisotropy between parallel and perpendicular directions will lead to excessive discretization errors unless some form of grid alignment is maintained. It is therefore recommended that the grid be kept as close as possible to an aligned, structured topology, using quadrilateral cells with two faces perfectly aligned with the flux surfaces, and two faces ‘as orthogonal as possible’ to the poloidal magnetic field. This is especially needed in the core and near-SOL regions. Not only will this limit the numerical error, it will also improve code stability and convergence properties compared to non-aligned cells by reducing the size and complexity of the stencil. The use of non-aligned faces and non-quadrangular cells should be limited to the areas where they are strictly needed, such as (a) in the vicinity of the walls (to resolve geometrical features and steep gradients towards the sheath), or (b) to reduce ‘bunching’ of field lines arising from an X-point or strongly shaped targets. In case triangles or pentagonal cells are included in the grid, optimal numerical performance is expected if these cells are within the same ‘discretized flux tube’ as their neighboring cells in the poloidal direction. For triangles, this means at least one of the triangle faces should be kept aligned with a flux surface.

3. Discretization of the governing equations on unstructured grids

The equations governing plasma transport in the unstructured B2.5 code follow the model described in Ref. [14], which has thus far also been the default model in the structured B2.5 code in SOLPS-ITER. The model includes continuity and parallel momentum equations for ions and (atomic) neutral species, and ion and electron internal energy equations. The condition that the divergence of the currents must be zero leads to an equation for the plasma potential. Parallel transport is classical, following Braginskii, while a typical diffusive approximation is used for the anomalous radial transport. The equations are solved in the 2D poloidal plane, assuming symmetry in the toroidal direction.

To describe the discretization of the governing equations, we base the discussion on a general nonlinear, anisotropic, convection–diffusion equation, following the notation introduced in Ref. [13]:

$$\frac{\partial u}{\partial t} + \nabla \cdot \mathbf{\Gamma} = S. \tag{1}$$

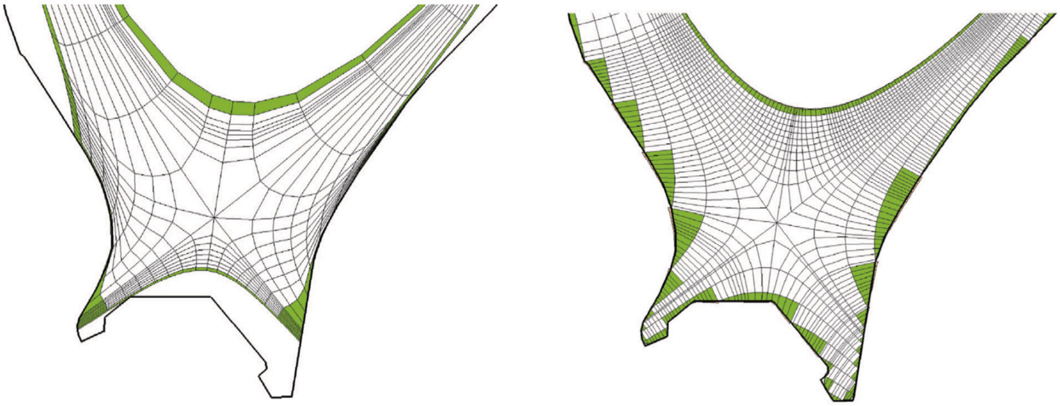

Fig. 1. Examples of ‘standard’ (left) and extended (right) AUG grids created by CARRE2 for SOLPS5. Figures reproduced from Ref. [9].

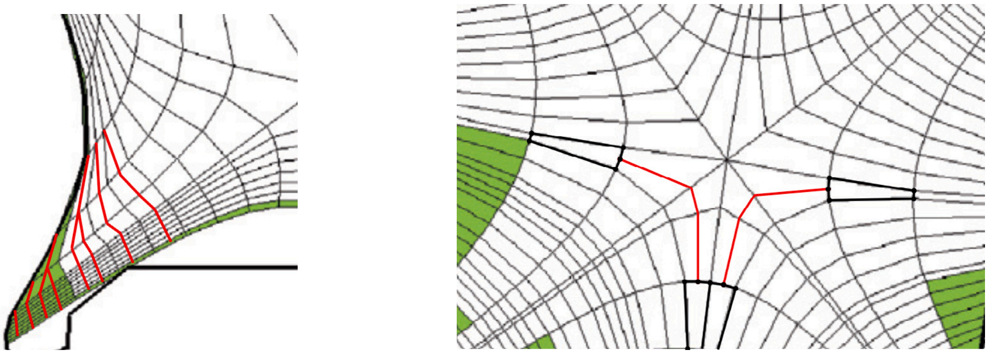

Fig. 2. Examples of refinement near targets (left), and near X-point (right) using internally unstructured grid topology. Red lines are additional grid lines used for local refinement compared to Fig. 1. In the right figure, cells that effectively became pentagonal are indicated with thick black contours. (For interpretation of the references to color in this figure legend, the reader is referred to the web version of this article.)

In this equation, u is a transported quantity, $\mathbf{\Gamma}$ the corresponding flux, and S a source term. The flux of a particular quantity follows a convection–diffusion prescription,

$$\mathbf{\Gamma} = \mathbf{C}u - \mathcal{D}\nabla u. \tag{2}$$

The anisotropy in the equations is most naturally expressed w.r.t. the poloidal and radial directions, which, by definition, are locally orthogonal to each other. We denote these directions by $\{\theta, r\}$, with respective unit vectors $\mathbf{e}_\theta$ and $\mathbf{e}_r$. In our notation, the poloidal direction points along the poloidal projection of the magnetic field, and the radial direction is orthogonal to it in the poloidal plane, forming a right-handed system with the third unit vector $\mathbf{e}_\phi$ along the toroidal projection of the field. These unit vectors therefore may flip orientation with poloidal/toroidal field reversal. The coefficient $\mathbf{C} = C_\theta \mathbf{e}_\theta + C_r \mathbf{e}_r$ in Eq. (2) is a vector describing the convective flux of u, with components defined in the poloidal and radial directions, and $\mathcal{D} = [D_{\theta\theta} D_{\theta r}, D_{r\theta} D_{rr}]$ is a diffusive tensor. The cross-diffusivities $D_{\theta r}$ and $D_{r\theta}$ are included because they are representative of the treatment of drift flows. Indeed, because in general drift flows have a form $\sim \nabla v \times \mathbf{B}$, with v some scalar field (e.g. pressure, electric potential, magnetic field strength,…), they have the same structure as a cross-diffusion term with $D_{\theta\theta} = D_{rr} = 0$ and $D_{\theta r} = -D_{r\theta} = D_{\mathrm{d}}$ [13].

In B2.5, the balance Eqs. (1) are discretized using a finite volume technique, which requires the evaluation of the fluxes in Eq. (2) across cell faces:

$$\begin{aligned}\mathbf{\Gamma} \cdot \mathbf{S} &= \Gamma_\theta S_\theta + \Gamma_r S_r, \\ &= \left(C_\theta u - D_{\theta\theta} \nabla_\theta u - D_{\theta r} \nabla_r u\right) S_\theta + \left(C_r u - D_{r\theta} \nabla_\theta u - D_{rr} \nabla_r u\right) S_r, \end{aligned} \tag{3}$$

where $\mathbf{S} = S_\theta \mathbf{e}_\theta + S_r \mathbf{e}_r$ is the surface vector of a face, expanded in its poloidal and radial components.

In an extended grids context, a cell face will in general not be aligned with either the poloidal or the radial directions. This is certainly true for the faces in direct contact with the walls (targets, main chamber, …), but also already in existing structured grids, because radial faces are usually distorted to match divertor targets. We therefore consider first a face arbitrarily oriented w.r.t. the magnetic field, see Fig. 3. The face under consideration is the thick solid line connecting vertices V_1 and V_2. C_1 and C_2 are the cell centers on either side of the face. The x-direction is defined through the (not necessarily straight) coordinate line connecting C_1 and C_2, going through the center of the cell face, and positive from C_1 to C_2. The y-direction is tangent to the face, positive from V_1 to V_2. The local coordinate system defined by x and y is in general curvilinear, and not orthogonal. γ is the complement of the angle between the x and y directions. The normal to the face, $\perp y$, is defined such that $\cos\gamma > 0$ (i.e. $-\pi/2 < \gamma < \pi/2$). For a face perpendicular to the connector line we have a locally orthogonal $\{x, y\}$ system, with $\gamma = 0$. Also at the face, we draw the local (orthogonal) poloidal and radial unit vectors. The orientation of the face w.r.t. the local magnetic field is given by the angle α between the poloidal magnetic field and the normal to the face. The angle $\beta = \gamma - \alpha$ between the x direction and the poloidal field direction is introduced for ease of notation below.

With these definitions, the typical faces that appear in structured grids are special instances of this general face description. For example, for a poloidal field clockwise from inner to outer target and toroidal field out of the page, we have that (1) an orthogonal ‘poloidal’ face between perfectly aligned cells has $\alpha = \beta = \gamma = 0$, $\mathbf{e}_x = \mathbf{e}_\theta$, $\mathbf{e}_y = \mathbf{e}_r$, (2) an aligned ‘radial’ face between perfectly aligned cells has $\alpha = \pi/2, \beta = -\pi/2, \gamma = 0$, $\mathbf{e}_x = \mathbf{e}_r$, $\mathbf{e}_y = -\mathbf{e}_\theta$, while (3) a ‘misaligned’ poloidal face between cells with aligned radial faces has $\alpha = \gamma, \beta = 0$, $\mathbf{e}_x = \mathbf{e}_\theta$ and (4) an aligned radial face between cells with ‘misaligned’ poloidal faces has

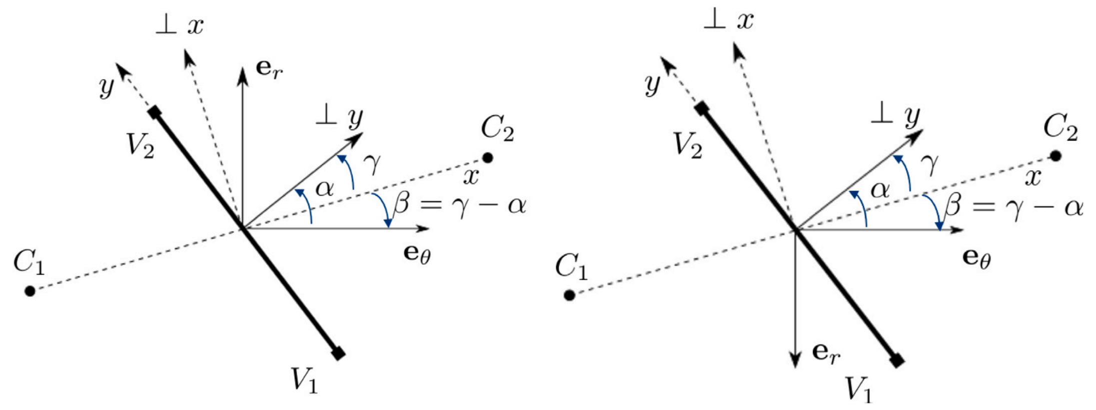

Fig. 3. Local coordinate systems defining cell face orientation w.r.t. magnetic field, cell centers, and vertices. Left: toroidal field out of page. Right: toroidal field into the page.

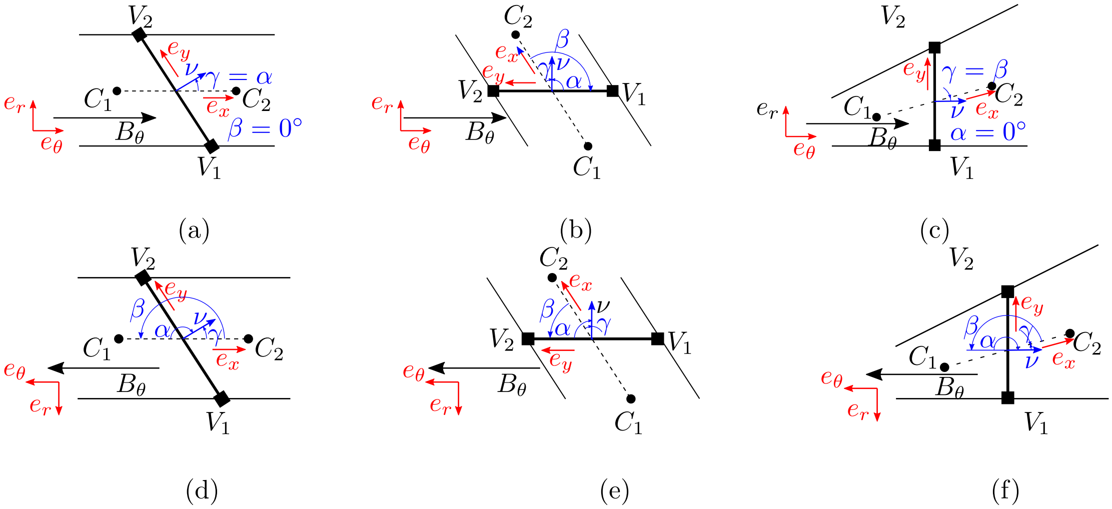

(a) (b) (c)

(d) (e) (f)

Fig. 4. Specification of face angles for a few representative configurations: (a) slanted poloidal face between cells with aligned radial faces; (b) aligned radial face between cells with slanted poloidal faces; (c) orthogonal poloidal face between cells with one radial face aligned with the poloidal field, and the other radial face aligned with the vessel boundary. (d)–(f): same cases, with reversed orientation of the poloidal field. Toroidal field out of the page.

$\alpha = \pi/2, \gamma \neq 0$, $\mathbf{e}_y = -\mathbf{e}_\theta$. Hence, our description here is a generalization of the one we presented in Ref. [13]. The definition of these face angles for a few typical cell configurations is illustrated in Fig. 4.

To compute the poloidal and radial components of the gradient required in Eq. (3), we relate them to the gradients in the x and y directions, which in turn can be computed directly from differences between cell center (for $\nabla_x u$) and vertex (for $\nabla_y u$) values of u. The desired expression for the components of the gradient can be obtained by expanding the gradient in the orthogonal poloidal–radial system, $\nabla u = \nabla_\theta u\, \mathbf{e}_\theta + \nabla_r u\, \mathbf{e}_r$, and applying the definition of the gradient, $\nabla_\mathrm{d} u = \nabla u \cdot \mathbf{d}$ for an arbitrary direction $\mathbf{d}$, to the unit vectors $\mathbf{e}_x$ and $\mathbf{e}_y$:

$$\begin{aligned}\nabla_x u = \nabla u \cdot \mathbf{e}_x &= \nabla_\theta u\, \mathbf{e}_\theta \cdot \mathbf{e}_x + \nabla_r u\, \mathbf{e}_r \cdot \mathbf{e}_x,\\ \nabla_y u = \nabla u \cdot \mathbf{e}_y &= \nabla_\theta u\, \mathbf{e}_\theta \cdot \mathbf{e}_y + \nabla_r u\, \mathbf{e}_r \cdot \mathbf{e}_y.\end{aligned}$$

From Fig. 3 we see that $\mathbf{e}_\theta \cdot \mathbf{e}_x = \cos\beta$, $\mathbf{e}_r \cdot \mathbf{e}_x = \mp \sin\beta$, $\mathbf{e}_\theta \cdot \mathbf{e}_y = -\sin\alpha$ and $\mathbf{e}_r \cdot \mathbf{e}_y = \pm\cos\alpha$, with the upper signs corresponding to toroidal field out of the page, and the lower signs with toroidal field into the page. Inverting the system, we obtain

$$\nabla_\theta u = \frac{\cos\alpha}{\cos\gamma}\nabla_x u + \frac{\sin\beta}{\cos\gamma}\nabla_y u, \tag{4}$$

$$\nabla_r u = \pm\frac{\sin\alpha}{\cos\gamma}\nabla_x u \pm \frac{\cos\beta}{\cos\gamma}\nabla_y u. \tag{5}$$

For completeness we give also the component of the gradient normal to the face, which is needed for some boundary conditions,

$$\nabla_\mathrm{n} u = \frac{1}{\cos\gamma}\nabla_x u + \frac{\sin\gamma}{\cos\gamma}\nabla_y u,$$

and note, trivially, that the component tangential to the face is the component in the y-direction: $\nabla_\mathrm{t} u = \nabla_y u$.

Computing the poloidal and radial components of the gradient in general thus requires a combination of gradients in x and y directions. The need for vertex values, which in turn are computed from cell center values using an appropriate interpolation scheme, leads to stencils that can become quite arbitrary and large, especially for grids including triangles. For example, structured grid areas with orthogonal, quadrangular cells lead to a standard 5-point stencil; structured grid areas with only misaligned poloidal faces give rise to a 9-point stencil [13]; the presence of an X-point typically leads to a 13-point stencil for the surrounding (quadrangular) cells, while the presence of triangles in the grid might lead to even broader stencils, since the number of cells connected to a single vertex is then no longer limited to 4. The unstructured solver fully accounts for this arbitrary number of points in the stencil, which leads to improved numerical stability. However, complex stencils also tend to slow down the matrix inversion process and require smaller time steps, which is why it is recommended to use as much as possible locally structured, orthogonal grid topologies.

Drift terms can also be discretized using the expressions above. Only the component of the drift perpendicular to a face leads to transport across a face. Recalling that drifts have the form of a cross-diffusion term in Eq. (3), the net drift flow $\boldsymbol{\Gamma}_{\mathrm{d}}$ across a face is of the form

$$\boldsymbol{\Gamma}_{\mathrm{d}} \cdot \mathbf{S} = -D_{\mathrm{d}} \left(\nabla_r u S_\theta - \nabla_\theta u S_r \right) = \mp D_{\mathrm{d}} \nabla_y u S, \tag{6}$$

where we use the identity $\mathbf{S} = (\cos\alpha\, \mathbf{e}_\theta \pm \sin\alpha\, \mathbf{e}_r)S$. Thus, net drift flow across the face depends only on gradients along the face, while the decomposition of the drift into its poloidal and radial components (as required for example for the collisions with neutrals) requires again the correct computation of the radial/poloidal gradients on each (possibly non-aligned) face.

Using the expressions for the fluxes and derivatives on faces given above, the governing equations can be discretized. Gradients in cell centers are obtained through interpolation of the cell face gradients. The discretization schemes of the structured version of the code have been generalized to arbitrary unstructured grids. Hybrid discretization schemes are used for the convection–diffusion flows, which are second order in space for diffusion-dominated flows, but tend to a first-order upwind scheme in convection-dominated flows.

The implementation guarantees exact backwards compatibility for original, structured, orthogonal grids. However, the discretization schemes of the unstructured solver no longer neglect effects of misalignment w.r.t. the magnetic field, and hence the solver is more accurate in realistic plasma edge geometries, even for non-extended grid cases. As demonstrated in Ref. [13], this is particularly important when using fluid neutral models. During the development of the new solver, various additional improvements to the numerical schemes were implemented. To avoid odd–even decoupling in the parallel direction due to the collocated velocity and density (pressure) fields, a Rhie–Chow scheme for compressible flow as described in Ref. [15] is implemented for the parallel direction. Flux limits for fluid neutrals now act on the total gradient-driven (particle or heat) fluxes, instead of only on the poloidal (for 'poloidal' faces) or radial (for 'radial' faces) components of the gradient as in the original code. This latter improvement removes an unwanted, artificial rotation of the flow direction due to the neutral flux limits in the original code. More details on the numerical scheme and related improvements will be presented in a companion paper. This same paper will present the results of the extensive verification that the solver has been (and is being) subjected to using the Method of Manufactured Solutions.

4. Generalized sheath boundary conditions

With grids extending to the wall along the entire plasma boundary, the need for artificial decay length or 'leakage' type BCs at outer flux surfaces is removed. At least in principle, we can now apply sheath BCs for the plasma at all vessel boundaries, thereby eliminating an important modeling uncertainty associated with existing simulations using structured grids. However, in any (2D) configuration there will always be areas in which the incidence angle of the field is extremely shallow (below a few degrees), or even purely tangential, where standard sheath theory breaks down and the Bohm–Chodura condition does not result in a meaningful prescription of the boundary condition. While the total extent of these areas – and hence their impact on the overall simulation results – is expected to be rather small in most cases, the equations do require a proper BC along the entire vessel. The investigation of the behavior of the sheath in (near) tangential conditions is an area of active research, and beyond the scope of the current work. Instead, we suggest a pragmatic generalization of the standard Bohm–Chodura conditions to a form applicable at all vessel boundaries, including truly tangential ones. More details on the BCs, including the reformulation of the BCs in presence of strong drifts, will be presented in the companion paper.

The standard Bohm–Chodura condition [16,17], already accounting for the possible effect of $E \times B$ drifts [18], states that the sum of plasma parallel and $E \times B$ velocities for a certain species a, projected normal to the surface must equal the plasma sound speed c_{s} times the projection of the field unit vector normal to the wall:

$$u_{\|,a}\mathbf{b} \cdot \boldsymbol{\nu} + \mathbf{V}^{E\times B} \cdot \boldsymbol{\nu} = u_{\|,a}\mathbf{b} \cdot \boldsymbol{\nu} \mp \frac{B_\phi}{B^2} \nabla_{\boldsymbol{\tau}} \varphi = \left| \mathbf{b} \cdot \boldsymbol{\nu} \right| c_{\mathrm{s}}, \tag{7}$$

with $\boldsymbol{\nu}$ defined as the outward normal at the boundary (i.e. pointing away from the plasma), $\boldsymbol{\tau}$ the local tangential direction to the surface, and $\mathbf{b}$ the unit vector along the magnetic field direction. φ denotes the electric potential. In a possible further generalization, the grad-B drift could also be included on the left-hand side of Eq. (7). This condition can be used as a boundary condition for the parallel velocity. Analyzing this equation first in the absence of drifts, it states that $u_{\|,a}\mathbf{b} \cdot \boldsymbol{\nu} = \left|\mathbf{b} \cdot \boldsymbol{\nu}\right| c_{\mathrm{s}}$. This imposes sound speed on the parallel velocity, but the condition is undetermined for the case of a perfectly tangential field ($\mathbf{b} \cdot \boldsymbol{\nu} = 0$). When drifts are included, the parallel velocity may need to be higher/lower than the local sound speed to compensate for a contribution of the $E \times B$ component normal to the boundary (determined by the gradient of the potential along the boundary). For the case of a purely tangential field, the condition actually becomes a condition on the potential, requiring that $\nabla_{\boldsymbol{\tau}}\varphi = 0$. For near-tangential conditions, extremely large parallel velocities may be required, especially if the $E \times B$ velocity is large. In any case, the Bohm–Chodura condition cannot be applied when the drift velocity is larger than two times the projected sound speed. Hence, both with and without drifts, we need a solution for grazing incidence. In the absence of an available theory, our pragmatic approach is to revert to a momentum leakage condition for the momentum flux $\boldsymbol{\Gamma}^{\mathrm{m}}$ if the incidence angle is below a minimal value:

$$\boldsymbol{\Gamma}^{\mathrm{m}} \cdot \boldsymbol{\nu} = -c^{\mathrm{m}} \frac{D}{\lambda} m_a n_a u_{\|,a}, \tag{8}$$

with D the anomalous diffusion coefficient, and m_a and n_a the mass and density of ions of species a. The decay length λ is an input parameter, representative of a turbulent characteristic length near the wall, and c^{m} is an input coefficient of order $\sim$1. Note that if $c^{\mathrm{m}} = 1$, and in combination with the prescription for the particle flux described below, this condition behaves as a Neumann condition for the parallel velocity.

For the continuity equation, we impose a particle flux normal to the wall corresponding to the Bohm condition (7), allowing also for an additional contribution from (isotropic) anomalous transport:

$$\boldsymbol{\Gamma} \cdot \boldsymbol{\nu} = \left|\mathbf{b} \cdot \boldsymbol{\nu}\right| n_a c_{\mathrm{s}} + \frac{D}{\lambda} n_a. \tag{9}$$

The second term provides for some leakage at true grazing incidence, and also some numerical stabilization. However, except at very grazing incidence or at very low temperatures, the anomalous term will generally be dominated by the 'regular' sheath contribution.

Boundary conditions for the ion and electron internal energy equations use standard sheath transmission coefficients to specify the internal energy fluxes ($\mathbf{Q}_{\mathrm{i/e}}$): $\delta_{\mathrm{i},1}$ for ions, and $\frac{1+\gamma_{\mathrm{e}}}{1-\gamma_{\mathrm{e}}}$ for electrons, accounting for secondary electron emission γ_{e}. Also here, the additional small leakage contribution to the particle fluxes enters, modeled with dedicated transmission coefficients $\delta_{\mathrm{i/e},2}$:

$$\mathbf{Q}_{\mathrm{i}} \cdot \boldsymbol{\nu} \;=\; \delta_{\mathrm{i},1} \left|\mathbf{b} \cdot \boldsymbol{\nu}\right| n_a c_{\mathrm{s}} T_{\mathrm{i}} + \delta_{\mathrm{i},2} \frac{D}{\lambda} n_a T_{\mathrm{i}}, \tag{10}$$

$$\begin{aligned} \mathbf{Q}_{\mathrm{e}} \cdot \boldsymbol{\nu} \;=\; & \left(\frac{1+\gamma_{\mathrm{e}}}{1-\gamma_{\mathrm{e}}} T_{\mathrm{e}} + e\varphi \right) \max\left(0, \left|\mathbf{b} \cdot \boldsymbol{\nu}\right| n_a c_{\mathrm{s}} - \frac{j_\|}{e} \mathbf{b} \cdot \boldsymbol{\nu} \right) \\ & + \left(\delta_{\mathrm{e},2} T_{\mathrm{e}} + e\varphi \right) \frac{D}{\lambda} n_a. \end{aligned} \tag{11}$$

Here, T_{i} and T_{e} are the ion and electron temperatures, $j_\|$ the parallel current, and e the unit of charge. For the ions, an additional option has been implemented to make the transmission coefficient $\delta_{\mathrm{i},1}$ consistent with the ion distribution function sampled on the EIRENE side, see below. In this case, it is no longer a free parameter.

Finally, the boundary condition for the potential equation is not modified compared to the standard sheath conditions:

$$\mathbf{j} \cdot \boldsymbol{\nu} = e \left(\left|\mathbf{b} \cdot \boldsymbol{\nu}\right| n_a c_{\mathrm{s}} - \left(1-\gamma_{\mathrm{e}}\right) \left|\mathbf{b} \cdot \boldsymbol{\nu}\right| n_{\mathrm{e}} \frac{1}{\sqrt{2\pi}} \sqrt{\frac{T_{\mathrm{e}}}{m_{\mathrm{e}}}} \exp\left(-\frac{e\varphi}{T_{\mathrm{e}}} \right) \right), \tag{12}$$

where **j** is the current.

The BCs described above are *ad hoc* generalizations of the standard Bohm–Chodura sheath conditions. Since the implementation in the code is still based on small *guard cells* at the boundaries, flexibility is maintained to impose various other BCs (Dirichlet, Neumann, Robin,…), as well as to further adapt or generalize the sheath conditions proposed here based on progressing insight into BCs for grazing field incidence.

5. Recycling model for kinetic neutral simulations

B2.5 is typically coupled to EIRENE [19,20] for a kinetic simulation of the neutral species. EIRENE itself is already fully adapted to simulations in complex geometries. However, in the interface with B2.5, some simplifying assumptions were made w.r.t. the grid structure, which have to be generalized for the new, unstructured solver.

The default recycling model used in SOLPS-ITER is described in Ref. [20]. At the magnetic pre-sheath entrance, EIRENE samples ions from a truncated drifting Maxwellian distribution function, where only velocity components $\mathbf{v}$ with $\mathbf{v} \cdot \boldsymbol{\nu} > 0$ are present in the distribution. The drift velocity and temperature of the truncated Maxwellian are determined by the ion fluid velocity and ion temperature at the sheath entrance, as computed by B2.5. These ions are then accelerated through the sheath potential and neutralized at the surface, after which various recycling models can be applied [20]. This coupling model has not been changed conceptually in the new extended grids framework, but has been generalized to arbitrary orientation of the recycling surfaces. In the process, some implicit assumptions in the interface have been lifted.

First, in the transfer of parallel/poloidal velocities from B2.5 to EIRENE, it was assumed that divertor targets were fully orthogonal to the poloidal field, which led to an artificial rotation of these velocities normal to the targets in the case of targets inclined w.r.t. the poloidal field. With the generalization of the geometrical description in the unstructured code version, this implicit assumption is readily removed.

Secondly, there was a discrepancy between the ion sheath transmission factor and the sheath potential drop used by both codes. The sheath potential drop in EIRENE was based on a model assuming zero currents through the sheath, while B2.5 does account for parallel currents, and possibly secondary electron emission, in the computation of the sheath potential. To correct this situation for the new unstructured grids, the sheath potential as computed by B2.5 is now passed to EIRENE for the acceleration of recycling ions. For the ion energy transmission coefficient, a similar though more subtle effect is present. The sampling of ions from a truncated Maxwellian distribution on the EIRENE side implies a certain (total) ion energy transmission coefficient. To ensure global energy conservation in the coupled code system, the ion sheath transmission factor can then no longer be set independently on the plasma side. Following Ref. [20], the total (internal + kinetic) ion sheath transmission coefficient $\delta_{\mathrm{i,t}}$ for this distribution is given by

$$\delta_{\mathrm{i,t}} = 2 + \mathcal{V}_\tau^2 + \mathcal{V}_\nu^2 + 0.5\,\frac{g(\mathcal{V}_\nu) - 1}{g(\mathcal{V}_\nu)}, \tag{13}$$

with $g(x) = 1 + \sqrt{\pi}x\,(1 + \mathrm{erf}(x))\exp(x^2)$, and $\mathcal{V} = Mc_{\mathrm{s}}/v_{\mathrm{T_i}}$ the normalized drift velocity. M is the Mach number, c_{s} the plasma sound speed, and $v_{\mathrm{T_i}} = \sqrt{2T_{\mathrm{i}}/m_{\mathrm{i}}}$ the ion thermal velocity that characterizes the width of the drifting Maxwellian distribution. Components of the normalized drift velocity normal and tangential to the wall are denoted as $\mathcal{V}_\nu$ and $\mathcal{V}_\tau$, respectively. For single-species plasmas with equal ion and electron temperatures and $M = 1$, this transmission coefficient depends only on the incidence angle of the field, varying between ~3.5 (normal incidence) and 3 (tangential field). In general, the exact value of the coefficient also depends on the ratio between ion and electron temperatures, and is species-dependent in multispecies plasmas. To implement this coefficient in B2.5, which solves an internal energy equation, the ion heat transmission coefficient $\delta_{\mathrm{i,1}}$ is specified indirectly through

$$\delta_{\mathrm{i,1}} = \delta_{\mathrm{i,t}} - Q_{\mathrm{k}} / \left(\left| \mathbf{b} \cdot \boldsymbol{\nu} \right| n_a c_{\mathrm{s}} T_{\mathrm{i}} \right), \tag{14}$$

with Q_{k} the flux of kinetic energy towards the sheath entrance.

The elimination of these hidden assumptions will lead to differences in the ion distributions reaching the surface compared to the structured code, even on existing structured grids, and hence also on the resulting neutrals. Hence, differences in solutions should also be expected when continuing existing cases with the new, unstructured SOLPS-ITER version. How significant these differences are will depend on the geometry and parameter settings used in the original case, but should be small in most cases.

With plasma grids extending to the main chamber and PF region walls, all neutrals are recycled from the true vessel boundaries, and no longer from the outermost flux surfaces. This is expected to have significant impact on the characteristics of main chamber recycling and sputtering [8]. Removal of the artificial internal recycling boundary can also influence the effective SOL opacity for recycled neutrals and therefore significantly influence the pedestal ionization source and H-mode density profile.

6. Simulations with realistic wall geometry

To test the newly developed code, we have performed a series of simulations on various grid types. A dedicated grid generator that can exploit all the features enabled by the new solver is under development at the ITER Organization. For our proof-of-principle study, we exploit existing grid generators. The test case is AUG 16151, a standard benchmark case for the SOLPS-ITER code. Three different grids are used: (1) a reference structured grid (available as part of the SOLPS-ITER repository), built with CARRE [21]; (2) a *target* mode grid, and (3) a *vessel* mode grid (see below for further details). Target and vessel mode grids were constructed with CARRE2 [9]. The grids are shown in Fig. 5.

The reference grid has 96 × 36 poloidal and radial cells. In the divertor area, cells are strongly distorted to match the targets. Good poloidal refinement towards the targets is achieved. However, due to the vertical target geometry, strong bunching of the grid lines near the top of the baffles can be noted.

The target mode grid is still a narrow grid. However, the cut-cell approach is used in the divertor, which leads to fully orthogonal cells in the interior of the simulation domain, but various trapezoidal and triangular cells near the target surface. In the vessel mode grid, the entire domain is gridded with orthogonal internal cells, with the cut-cell approach used along the full vessel boundary. For these two grids, the problem of bunched field lines near the top of the baffles is avoided. The orthogonal cells also result in predominantly 5-point stencils, which help convergence compared to the strongly distorted cells in the reference grid. However, with the cut-cell approach it is very difficult to achieve good poloidal refinement towards vessel boundaries (which is essential to numerically resolve plasma acceleration towards the sheath) without drastically increasing the number of cells. This is especially problematic for the full vessel grid, where a very fine poloidal resolution is needed in the entire domain in order to properly resolve all remote wall features.

The resulting target and vessel mode grids have 7018 resp. 14726 cells, and were constructed from orthogonal, structured base grids with 303 × 25 and 432 × 106 poloidal and radial cells respectively. The vessel mode grid contains exactly the same flux surfaces as the target mode grid, with additional surfaces added to resolve the entire main chamber and private flux regions. Poloidal resolution in the divertor is similar for both grids (but not identical, because it is the result of an automated CARRE2 procedure [9]). Despite the already high poloidal resolution of the vessel mode grid, some cells with insufficient poloidal resolution still remain in some remote areas and pose difficulties for the convergence of the simulations on this grid.

The simulations reported below have been performed for a deuterium-only plasma, both with fluid neutrals and with a full kinetic EIRENE model (incl. molecules and neutral–neutral collisions). The potential equation is not solved (and hence drifts and currents are not

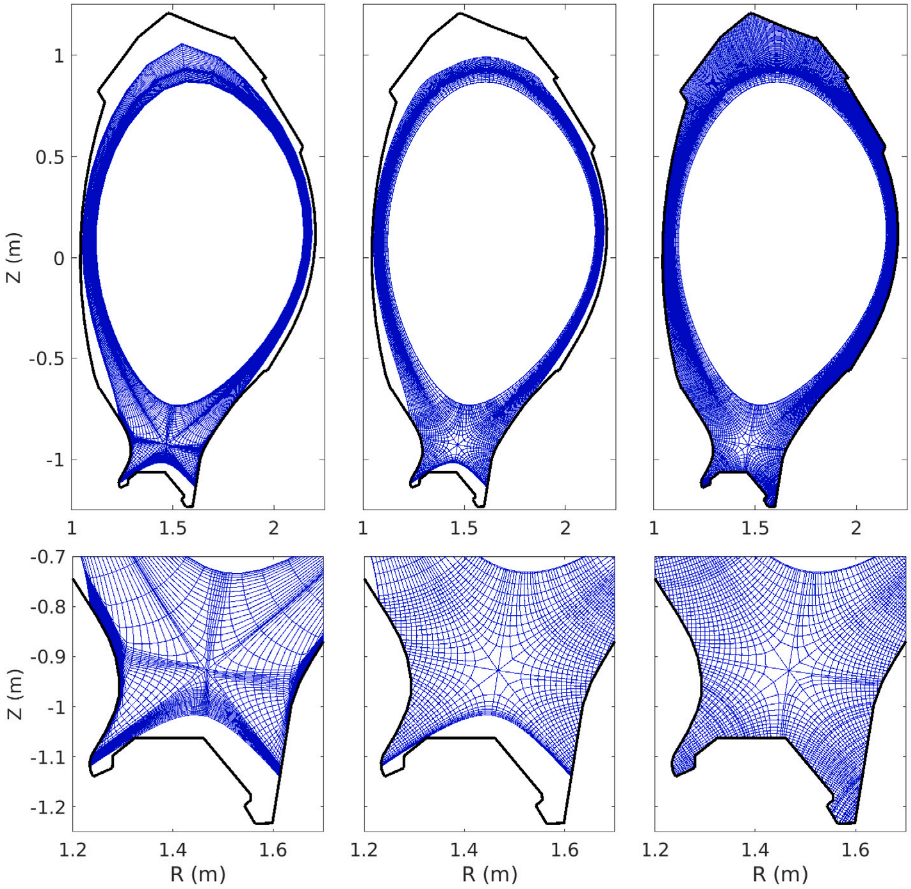

Fig. 5. AUG grids, including zoom of the divertor area. Left: reference structured grid; middle: *target mode* grid; right: *vessel mode* grid.

included), mainly because at present it remains difficult to solve the potential equation in full vessel mode. We expect that this problem will at least partially be resolved by improved gridding techniques providing better resolution of detailed wall features. We note that simulations including potential equation, currents, and drifts have been performed successfully with the target mode grid.

The simulation with kinetic neutrals presented below represents the first coupled B2(.5)-EIRENE simulation with an extended grid. We use this simulation mainly to illustrate qualitative agreement with fluid neutral simulations in the extended grids context. Earlier benchmark studies have usually found strong qualitative and quantitative differences between fluid and kinetic neutral simulations, but it is often hard to quantify to which extent these differences come from kinetic effects or geometrical details. Indeed, in practice non-extended B2(.5)-EIRENE simulations have the plasma restricted to an outermost flux surface, while the neutral grid does fill the entire main chamber (and divertor) volume up to the vessel. Non-extended B2.5 simulations with fluid neutrals, on the other hand, also have the fluid neutral population restricted to the plasma grid. We find that fluid and kinetic neutral simulations show very reasonable qualitative agreement on extended grids (i.e. when both are simulated on exactly the same geometry). At the same time, the differences between solutions on extended and non-extended domains with fluid neutrals confirm the necessity to take the full vessel geometry into account in plasma edge simulations.

At the core boundary, we impose a fixed plasma density of $2 \cdot 10^{19}$ m^{-3}, fixed $T_\mathrm{i} = T_\mathrm{e} = 275$ eV, zero parallel velocity, and zero neutral particle flux. For the vessel mode simulation, sheath conditions are applied at the entire wall boundary, imposing $M = 1$ for the parallel velocity at the sheath entrance, and an ion parallel sheath transmission coefficient of $\delta_{\mathrm{i},1} = 2.5$. The anomalous leakage parameters have been set to $\lambda = 0.1$ m, $\delta_{\mathrm{e},2} = 2.5$, and $\delta_{\mathrm{i},2} = 5$ at the main chamber boundary, but are not used at the target/baffle boundaries since the incidence angles in the current setup do not require the additional stabilization. The anomalous particle diffusion coefficient and ion/electron conductivities are set at $D = 0.4$ m^{2}s^{-1} and $\chi_{\mathrm{i,e}} = 1.6$ m^{2}s^{-1}. A recycling coefficient of 1 is imposed along the entire boundary. In the absence of puff and pump, we thus have a closed system for mass/particles.

For the non-extended (‘narrow’) reference and target mode grids, we use the same core boundary conditions and sheath conditions at the targets as for the vessel mode grid, as well as identical transport coefficients and recycling coefficients. At the outermost radial boundary, leakage parameters were tuned manually to achieve approximately the same radial profiles of density and temperatures compared to the full extended grid simulation at the outer midplane.

6.1. Main chamber solution

The ability to simulate up to the main chamber wall has removed the need for an artificial boundary condition at the outermost magnetic flux surface. Matching experimental profiles of density and temperatures at the outer midplane traditionally requires tuning both radial profiles of transport coefficients *and* decay length, or leakage BCs, since both have a strong impact on the simulated profiles. Similar density and temperature profiles can usually be obtained with different combinations of BCs and transport coefficients. With a grid extending to the wall, an important free parameter is eliminated from the model, where now only transport coefficients are available to achieve relevant solutions.

In the simulations presented here, we have used the extended grid simulation as a reference to tune the leakage BCs of the narrow grid simulations, aiming to achieve the same profiles at the outer midplane.

Both simulations have identical transport coefficients. Note that in the narrow grid simulations, these leakage parameters are then taken poloidally constant along the outermost boundary. In contrast, by postprocessing the results of the extended grid simulation, we find a variation of up to a factor 2 in the 'effective' leakage parameter at this flux surface. The resulting electron density profiles at the inner and outer midplane on the various grids are shown in Fig. 6, for the cases with fluid neutrals. We remark that while the agreement at the outer midplane is excellent between all grids, some notable differences in the profiles are seen at the inner midplane. At this location, the profiles of standard and target-mode grids almost exactly coincide — as expected since both are non-extended cases. Note that for the standard grid, the effects of grid distortion near the targets are now fully accounted for by the numerical scheme. Especially for fluid neutral simulations, this is absolutely essential. Neglecting grid distortion effects would lead to qualitatively and quantitatively incorrect results, as already reported in Ref. [13]. The remaining small differences in the profiles between standard and target-mode grids are ascribed to discretization effects. However, the density profile of the fully extended grid shows a peak in the density profile at the inner midplane as well as a slight broadening compared to the other cases. This is a result of local recycling effects near the inner tangency point (see below), an effect only captured by the extended vessel mode grid.

Fig. 7 compiles 2D distributions of the Mach number from the simulations. Since the results on the standard and target mode grids are nearly identical, only the results on the new target mode grid are shown, along with the Mach number on the extended vessel mode grid for both fluid and kinetic neutral simulations. Positive Mach numbers indicate flow in the (positive) magnetic field direction, which has a counter-clockwise poloidal component in these simulations. The figures nicely illustrate that for the extended grids outflow with Mach number 1 is reached at all vessel boundaries, as imposed by the sheath boundary conditions. Some insufficiently resolved areas (cells with large poloidal width) are also visible near the top of the vessel for the extended cases. Improved grid generation techniques are needed to better resolve the solution in these regions. In the near SOL, the Mach number profiles are qualitatively very similar. Still there is a difference in the range of 10 % between target and vessel mode solutions in almost the entire near SOL, with peaks up to 50% in the (inner) divertor.

The main chamber fluxes resulting from the plasma flow patterns of Fig. 7 are illustrated in Fig. 8. It shows the particle, electron and ion heat fluxes along the main chamber wall, from the top of the inner baffle clockwise to the top of the outer baffle (fluxes in the divertor region are not included), for target and vessel mode grids. In the narrow grid simulation, the radial plasma fluxes at the outermost flux surface are interpreted as estimates for the main chamber loading using a 'teleportation' ansatz, resulting in rather smooth profiles of the particle and heat loads. The ability to simulate beyond this outermost flux surface in the extended cases leads to a significant redistribution of the plasma fluxes. Indeed, beyond the outermost flux surface of the narrow grids the plasma still predominantly follows the magnetic field. Therefore, the main chamber loads are poloidally concentrated on narrow regions where the wall is 'magnetically closest' to the separatrix (the inner midplane, the outer midplane, and near the top of the baffles), while recessed wall areas receive almost no plasma (and recycling) fluxes. The 'spike' in the wall loads around $s \sim 3.2$ m is located just above the outer midplane, where due to a local feature in the vessel geometry the wall is nearly orthogonal to the poloidal field. Similar observations were already made in Ref. [7], for standalone extended B2 simulations. Note that even if we would use the 'effective' leakage parameters from the wide grid simulation as a boundary condition for the narrow grid simulation, the results would still differ significantly because this far SOL plasma transport cannot be captured by the narrow grids. Similarly, in the usual approach in which kinetic neutral simulations do extend to the main chamber, despite a limited radial extent of the plasma grid, this poloidal redistribution of the plasma fluxes cannot be captured.

The poloidally localized plasma fluxes also result in a poloidal redistribution of the neutral recycling processes in the main chamber. We illustrate this by comparing the plasma particle sources due to recycling in Fig. 9. Note that the scale in the figure is limited to the maximum of the sources in the main chamber; the magnitude of the recycling sources in the divertor is at least an order of magnitude larger. The noisy results for the case with kinetic neutrals are due to the rather small (but sufficient) number of neutral trajectories used in this study.

For the narrow grid case, the plasma sources are distributed quite smoothly in the poloidal direction, since neutrals recycle back into the plasma directly from the smoothly distributed plasma flux at the outermost flux surface. Main chamber recycling is somewhat larger near the outboard side of the machine in the narrow grid case, as a result of the larger plasma fluxes there, in turn due to the larger area compared to the high-field side. In contrast, for the extended grid simulations, main chamber recycling is poloidally clearly concentrated in a few distinct areas: the inner midplane, the outer midplane, and near the top of the baffles. These are again the regions which are magnetically closest to the separatrix, and receive the largest plasma fluxes. Note that the effect of recycling at the top of the inner baffle is already partially captured by the narrow grid, because in this particular case the narrow grid extends quite far up on the inner baffle. While it is not very obvious from the figures, the outermost flux surface of the narrow grid is almost exactly tangential to the upper part of the outer baffle, and only intersects the outer baffle at approximately the same Z-coordinate as at the inner baffle. This explains why the intense recycling at the top of the outer baffle is missed by the narrow grid simulation. Note that the poloidal distribution of the neutrals in the main chamber (not shown) qualitatively resembles the distribution of the plasma sources: they are also clearly localized in the same poloidal regions, with very few neutrals at all near the top of the machine in the extended grid simulations. The impact of these observations on far-SOL flows remains to be assessed.

We note that apart from the poloidally localized recycling (and associated sputtering) patterns, there is a second effect of extended grid simulations on the energy spectra of neutrals impacting the main chamber, as assessed in Ref. [8] using a fixed plasma background. That study concluded that the neutral energy spectra at the main chamber wall are more biased towards lower energies in extended grid simulations. This is a result of recycling neutrals being born further away from the main plasma (i.e. directly at the vessel wall), where the far SOL plasma is colder. Moreover, the far SOL plasma tends to screen these cold neutrals more effectively from the near SOL and core regions, leading to reduced energies of CX neutrals reaching the main chamber walls compared to simulations on non-extended grids. In contrast, neutrals in narrow-grid simulations directly recycle back into the plasma from the outermost simulated flux surface, with higher initial energies and closer to the hotter near SOL plasma.

6.2. Divertor solution

Finally, we analyze the solutions in the divertor. As for the main chamber – and since the numerical scheme correctly accounts for grid distortion – the differences between standard and target mode grids are small, so we only compare the latter to extended grid simulations.

Fig. 10 shows the electron (top) and neutral (bottom) densities for target mode and vessel mode grids with fluid neutrals, and for vessel mode grid with kinetic neutrals. On the rightmost figures, the relative differences between narrow and extended grid solutions with fluid neutrals are shown. Note that these relative differences are only available on the narrow grid region covered by both simulations. For visibility, we have limited the scale between -1 and 1 for the relative error, but we remark that the relative errors show peaks up to a factor $\sim \pm 2.5$ in the divertor area. Clearly, all three solutions are qualitatively quite

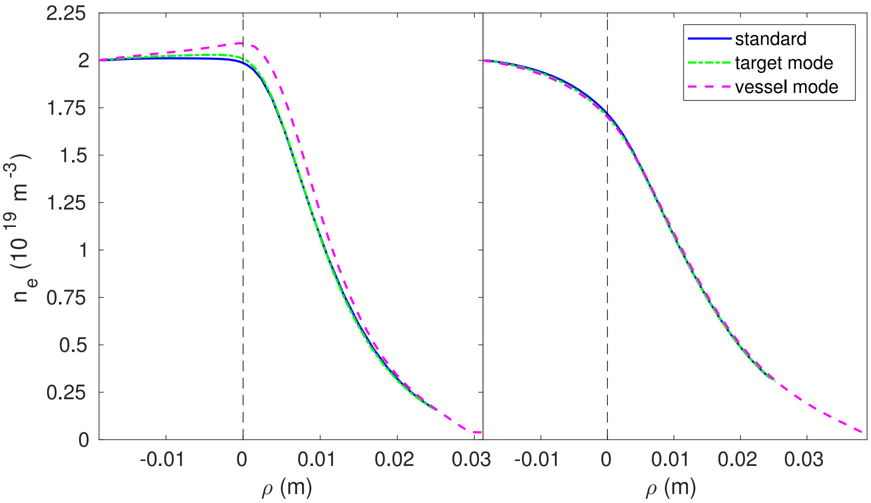

Fig. 6. Electron density profiles at inner (left) and outer (right) midplane, mapped to the outer midplane, for the different grids in Fig. 5. Cases with fluid neutrals.

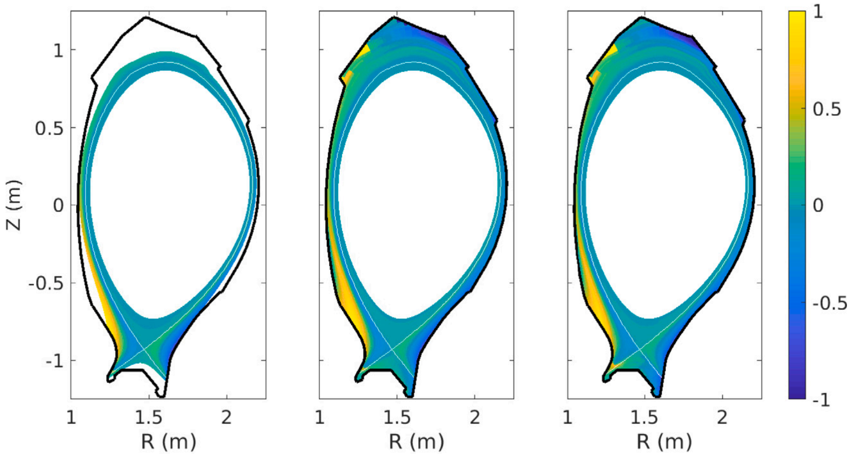

Fig. 7. Mach number. From left to right: *target mode* solution; *vessel mode* solution; *vessel mode* solution, kinetic neutrals.

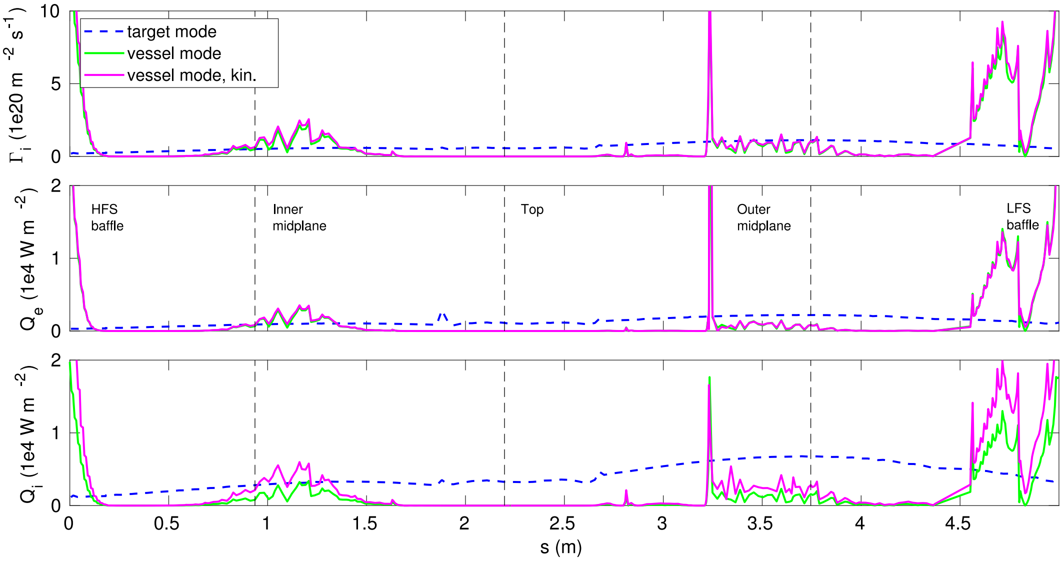

Fig. 8. Main chamber fluxes, ranging from top of the inner divertor baffle (left) to outer baffle (right) for the target and vessel mode grids. Top: particles; middle: electron internal energy; bottom: ion internal energy.

similar, predicting roughly the same inner–outer divertor asymmetry and neutral compression patterns (note: drifts not included). We remark

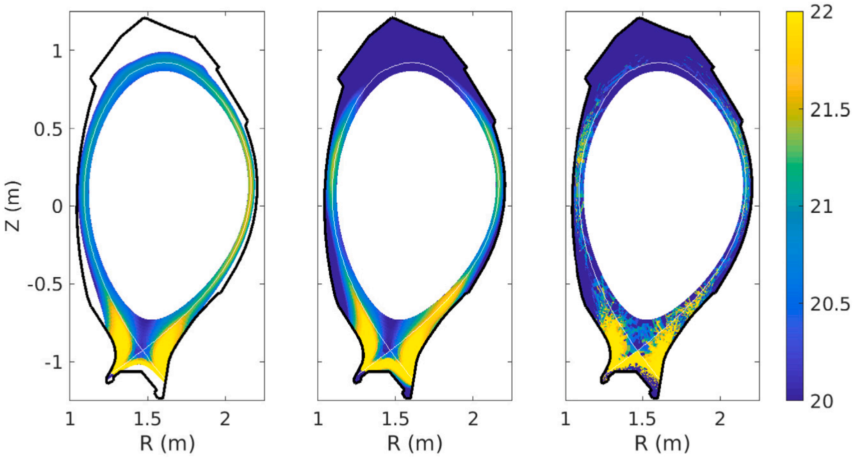

Fig. 9. Particle source due to recycling ($m^{-3}s^{-1}$, log10 scale). Left: *target mode* solution; middle: *vessel mode* solution; right: *vessel mode* solution, kinetic neutrals.

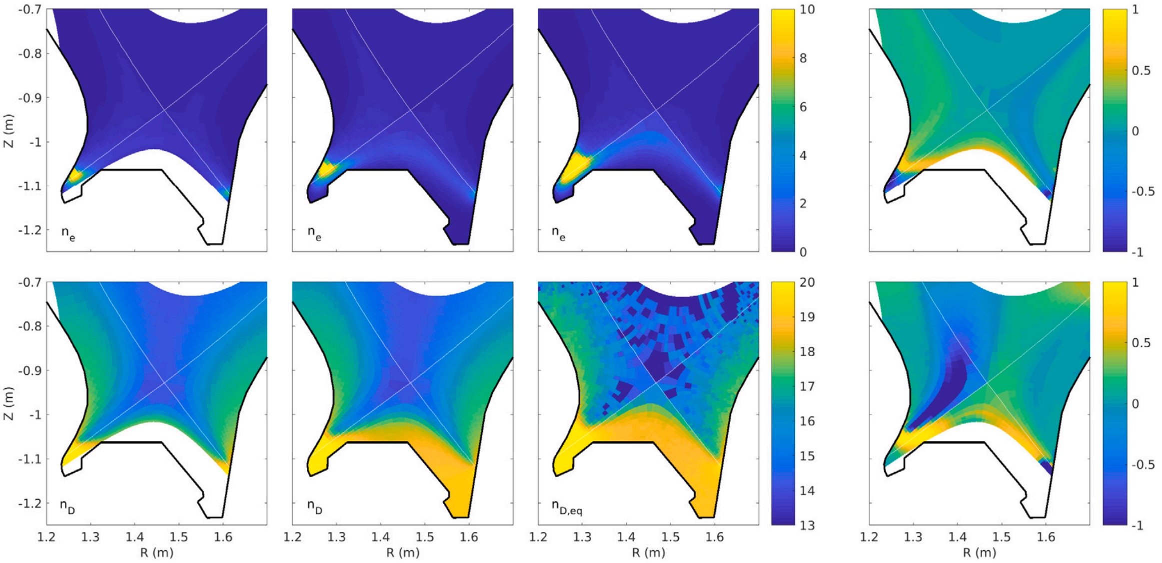

Fig. 10. Electron density (10^{21} m^{-3}, top) and neutral density (log10 scale, bottom) for, from left to right: *target mode* grid; *vessel mode* grid with fluid neutrals; *vessel mode* grid with kinetic neutrals. The rightmost figures show the relative difference between target and vessel mode solutions with fluid neutrals. Note that for the kinetic neutral case, we show the 'equivalent' atomic density $n_{D,eq} = n_D + 2n_{D_2}$, with n_D the atomic and n_{D_2} the molecular density.

in particular that both fluid neutral solutions are qualitatively (but not quantitatively) similar to the simulation with kinetic neutrals, which includes among others molecules and neutral–neutral collisions. Still, both extended grid solutions show a few features not present in the narrow grid solution. For example, the extended solutions are able to capture the presence of (plasma and) neutrals in the 'void' private flux region, which enables communication between inner and outer divertors, and leads to some recycling on the top of the structure between inner and outer divertor legs (near the point where that structure touches the outer surface simulated by the non-extended grid). In this particular case the inner target geometry is quite 'closed', with the narrow grid already capturing the closure quite well. Still, for nearly identical outer midplane conditions, the extended simulations do predict somewhat denser inner divertor conditions compared to the narrow grid solution.

For completeness, we also show the particle and heat loads to the inner and outer targets in Fig. 11. The figures confirm that the fluxes near the strike zones are not impacted too strongly by the extended grids in this case study. Especially at the outer target the target and vessel mode solutions with fluid neutrals are very similar. At the inner target, the vessel mode profiles are indicative of higher recycling conditions than in the narrow grid, consistent with the observation of increased plasma and neutral densities (and correspondingly lower temperatures) in that region (Fig. 10). Although we do not show the results here, we note also that the most protruding part of the structure between the divertor legs receives ion and electron heat fluxes of the same order as those at the top of the baffles, and particle fluxes of the order of $1 \cdot 10^{22}$ $m^{-2}s^{-1}$.

7. Conclusion

In this paper we have presented the new unstructured finite volume solver that has been implemented in the B2.5 plasma transport code within SOLPS-ITER. The new solver enables 2D plasma edge simulations extending to the true vessel boundaries, providing extensive flexibility to resolve detailed wall features, as well as arbitrary (advanced) magnetic topologies. Generalized sheath boundary conditions are presented that can be applied at any magnetic field incidence angle. The consistent coupling with EIRENE for simulations with kinetic neutrals is described.

The newly developed solver has been applied to a standard AUG benchmark case for SOLPS-ITER, and results both in the main chamber

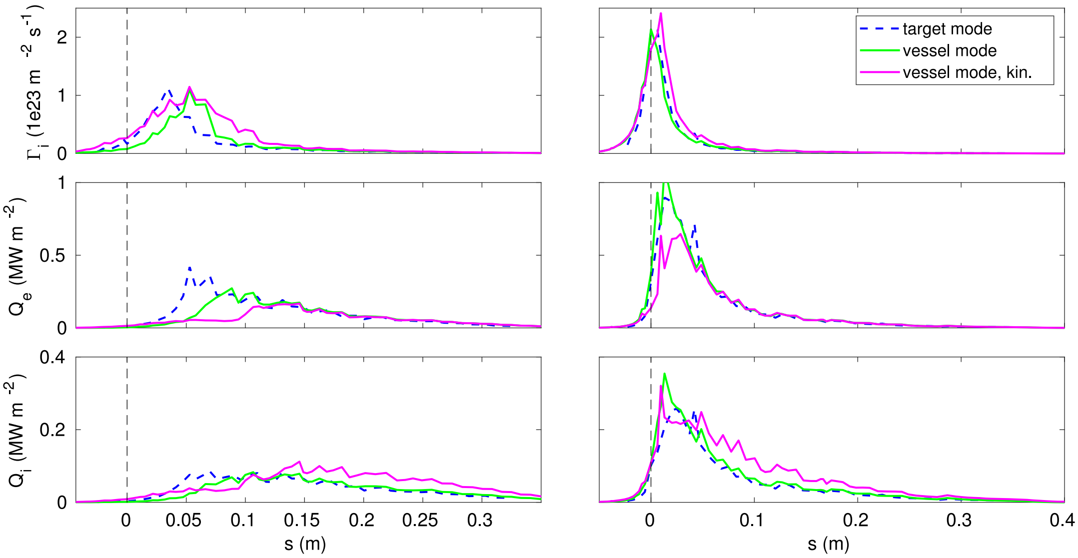

Fig. 11. Inner (left) and outer (right) target fluxes. Top: particles; middle: electron internal energy; bottom: ion internal energy.

and divertor have been compared with standard simulations on non-extended grids. With the new solver, poloidally localized main chamber loading and recycling patterns can now be captured. The resulting plasmas can form the basis for studies of far SOL flows, as well as main chamber recycling, erosion, and material migration studies. Taking into account the details of the divertor geometry afforded by the new wide grids is also shown to be important for the details of the divertor plasma solution. Moreover, the extended grids functionality leads to an improved agreement between fluid neutral and kinetic neutral simulations. While we have not analyzed this agreement quantitatively, the qualitative agreement obtained here is already very promising with regard to the further development of advanced fluid and hybrid neutral models [22–24] which match well with kinetic neutral simulations in high recycling and detached conditions.

To further exploit the benefits of the new solver, grid generation techniques to accurately resolve the wall features without unnecessarily increasing grid resolution in the entire simulated domain need to be pursued. Presently, the TIARA grid generation tool is being developed at ITER for that purpose.

Declaration of competing interest

The authors declare that they have no known competing financial interests or personal relationships that could have appeared to influence the work reported in this paper.

Acknowledgments

This work was funded in part by ITER service contract IO/17/CT/4300001523. The views and options expressed herein do not necessarily reflect those of the ITER Organization. Parts of the work were supported by the Research Foundation Flanders (FWO) under project grant G078316N.

References

[1] S. Wiesen, D. Reiter, V. Kotov, et al., J. Nucl. Mater. 463 (2015) 480–484.
[2] X. Bonnin, W. Dekeyser, R.A. Pitts, et al., Plasma Fusion Res. 11 (2016) 1403102.
[3] A.S. Kukushkin, H.D. Pacher, V. Kotov, et al., Fusion Eng. Des. 86 (2011) 2865–2873.
[4] R.A. Pitts, X. Bonnin, F. Escourbiac, et al., Nucl. Mater. Energy 20 (2019) 100696.
[5] F. Militello, et al., These proceedings.
[6] F. Nian, J. Chen, Z. Yang, et al., Paper MF-O16, in: 3rd Asia-Pacific Conference on Plasma Physics, Hefei, China, 2019.
[7] M. Baelmans, P. Boerner, W. Dekeyser, et al., Nucl. Fusion 51 (2011) 083023.
[8] W. Dekeyser, M. Baelmans, D. Reiter, et al., J. Nucl. Mater. 415 (1) (2011) S584–S588.
[9] H.-J. Klingshirn, D.P. Coster, X. Bonnin, J. Nucl. Mater. 438 (2013) S856–S860.
[10] H. Bufferand, B. Bensiali, J. Bucalossi, et al., J. Nucl. Mater. 438 (2013) S445–S448.
[11] G. Giorgiani, H. Bufferand, G. Ciraolo, et al., J. Comput. Phys. 374 (2018) 515–532.
[12] I.S. Landman, Tokamak code TOKES, models and implementation, Forschungszentrum Karlsruhe report FZKA 7496, 2009, see https://publikationen.bibliothek.kit.edu/1000022049.
[13] W. Dekeyser, X. Bonnin, S.W. Lisgo, et al., Nucl. Mater. Energy 18 (2019) 125–130.
[14] V. Rozhansky, E. Kaveeva, P. Molchanov, et al., Nucl. Fusion 49 (2009) 025007.
[15] F. Moukalled, L. Mangani, M. Darwish, The Finite Volume Method in Computational Fluid Dynamics, Springer, Switzerland, 2016.
[16] D. Bohm, in: A. Guthrie, R.K. Wakerling (Eds.), The Characteristics of Electrical Discharges in Magnetic Fields, McGraw-Hill, New York, 1949 (Ch. 3).
[17] R. Chodura, in: D.E. Post, R. Behrisch (Eds.), Physics of Plasma-Wall Interactions in Controlled Fusion, Plenum Press, New York, 1986.
[18] P.C. Stangeby, The Plasma Boundary of Magnetic Fusion Devices, IOP Publishing, Bristol and Philadelphia, 2000.
[19] D. Reiter, M. Baelmans, P. Boerner, Fusion Sci. Technol. 47 (2005) 172–186.
[20] D. Reiter, The EIRENE code user manual, available from http://www.eirene.de.
[21] R. March, M. Dumberry, Comput. Phys. Comm. 96 (1996) 232–246.
[22] M. Blommaert, W. Dekeyser, N. Horsten, et al., Contrib. Plasma Phys. 58 (2018) 718.
[23] W. Van Uytven, M. Blommaert, W. Dekeyser, et al., Contrib. Plasma Phys. 60 (2020) e201900147.
[24] N. Horsten, W. Dekeyser, M. Blommaert, et al., Contrib. Plasma Phys. 60 (2020) e201900132.